Unsteady flows in Io's atmosphere caused by condensation and sublimation during and after eclipse: Numerical study based on a model Boltzmann equation

Shingo Kosuge[a,*], Kazuo Aoki[a], Takeshi Inoue[a], David B. Goldstein[b], Philip L. Varghese[b]

[a] *Department of Mechanical Engineering and Science and Advanced Research Institute of Fluid Science and Engineering, Graduate School of Engineering, Kyoto University, Kyoto 606-8501, Japan*

[b] *Department of Aerospace Engineering and Engineering Mechanics, The University of Texas at Austin, 1 University Station, C0600, Austin, TX 78712, USA*

Abstract

The behavior of Io's atmosphere during and after eclipse is investigated on the basis of kinetic theory. The atmosphere is mainly composed of sulfur dioxide (SO_2) gas, which condenses to or sublimates from the frost of SO_2 on the surface depending on the variation of surface temperature ($\sim$ 90–114K). The atmosphere may also contain a noncondensable gas, such as sulfur monoxide (SO) or oxygen (O_2), as a minor component. In the present study, an accurate numerical analysis for a model Boltzmann equation by a finite-difference method is performed for a one-dimensional atmosphere, and the detailed structure of unsteady gas flows caused by the phase transition of SO_2 is clarified. For instance, the following scenario is obtained. The condensation of SO_2 on the surface, starting when eclipse begins, gives rise to a downward flow of the atmosphere. The falling atmosphere then bounces upward when colliding with the lower atmosphere but soon falls again. This process of falling and bounce back of the atmosphere repeats during the eclipse, resulting in a temporal oscillation of the macroscopic quantities, such as the velocity and temperature, at a fixed altitude. For a pure SO_2 atmosphere, the amplitude of the oscillation is large because of a fast downward flow, but the oscillation decays rapidly. In contrast, for a mixture, the downward flow is slow because the noncondensable gas adjacent to the surface hinders the condensation of SO_2. The oscillation in this case is weak but lasts much longer than in the case of pure SO_2. The present paper is complementary to the work by Moore et al. (Icarus 201, 585–597) using the direct simulation Monte Carlo (DSMC) method.

Keywords: Io; Eclipses; Jupiter, satellites; Satellites, atmosphere; Atmosphere, dynamics

1. Introduction

Io, one of the satellites of Jupiter, has not only extremely active volcanos but also a unique atmosphere mainly composed of sulfur dioxide (SO_2) gas (Kliore et al., 1975; Pearl et al., 1979; Lellouch et al., 1990; Ballester et al., 1994; Spencer et al., 2000). During the night, the surface temperature of Io drops to about 90 K (except around the volcanos) and the SO_2 gas condenses to form a very thin layer of frost on the ground (Fanale et al., 1979; Howell et al., 1989; Douté et al., 2001). Then the atmosphere almost vanishes. Conversely, the atmosphere is restored during the daytime, when the surface temperature rises to about 120 K due to the increase of insolation and the surface frost sublimates (Jessup et al., 2004; Geissler et al., 2004; Spencer et al., 2005; Retherford et al., 2007).

A number of early models of Io's atmosphere were based on continuum gas dynamics and considered a steady flow of SO_2 sublimating in the dayside hemisphere and condensing in the nightside hemisphere (Ingersoll et al., 1985; Ingersoll, 1989; Moreno et al., 1991; Strobel et al., 1994; Wong and Johnson, 1995, 1996; Wong and Smyth, 2000; Smyth and Wong, 2004). The effect of rarefaction was taken into account for the first time by Austin and Goldstein (2000). They carried out a numerical analysis of the above steady flow based on the Boltzmann equation using the direct simulation Monte Carlo (DSMC) method. The same DSMC method was subsequently applied to analyses of the behavior of volcanic plumes (Zhang et al., 2003) and of the whole 3-D atmosphere (Walker et al., 2010).

The atmospheric collapse and reconstruction are also expected to take place during and after eclipse, when Io enters into the shadow of Jupiter (Retherford et al., 2007). Recently, Moore et al. (2009) applied the DSMC method to the analysis of 1-D unsteady behavior of an atmospheric column above a specific point on Io during eclipse. As a result, they revealed that the behavior may be significantly influenced by a trace of noncondensable gas [SO or O_2;

*Corresponding author.
Email address: kosuge.shingo.6r@kyoto-u.ac.jp (Shingo Kosuge)

see Lellouch et al. (1996); de Pater et al. (2002)] contained in the atmosphere as a minor component.

The approach by Moore et al. (2009) may be extended in two different directions: One is to perform 3-D computations with various real effects, such as plasma-induced chemistry and electric and magnetic fields, and the other is to focus attention, with suitable simplifications, on a specific effect that was found to be important. The first approach can explain the observed data and predict real phenomena, whereas the second approach may reveal underlying basic physical and gasdynamic mechanisms that were not explored in Moore et al. (2009). Both approaches are important and complementary. The first approach is taken by the recent paper by Walker et al. (2012) [see also Walker (2012)], while the present paper is devoted to the second approach with special attention paid to the effect of the noncondensable gas.

In the present study, we consider the same 1-D problem as in Moore et al. (2009) after making some simplifications. More specifically, in order to concentrate on the dominant effect of the noncondensable gas, we omit other effects, such as those of the Io plasma torus, atmospheric radiative cooling, and molecular internal structure, considered in Moore et al. (2009), and those of strong lateral winds and of chemical or photochemical reactions occurring in the real atmosphere.

Our aim is to describe time evolution of the profiles of physical quantities in detail for sufficiently long time intervals. For this purpose, the DSMC method used in Moore et al. (2009) may be excessively costly because of its well-known weakness for unsteady problems originating from the inherent statistical noise. However, alternative methods have also been developed in the field of rarefied gas dynamics, which can be suitably exploited depending on the situation and purpose. We adopt, in place of the full Boltzmann equation, a model Boltzmann equation of Bhatnagar-Gross-Krook (BGK) type (Bhatnagar et al., 1954; Welander, 1954) for a gas mixture, proposed in Andries et al. (2002), and perform an accurate numerical analysis using a finite-difference method, which is free from stochastic noise. As the result, we obtain detailed information on the time evolution of physical quantities that is not available from Moore et al. (2009). For instance, we find some new interesting phenomena, such as an oscillatory motion in the atmosphere at intermediate altitudes caused by successive falling and bounce back of the atmosphere during eclipse.

2. Description of problem and numerical analysis

2.1. Problem and assumptions

Consider an atmospheric column over a fixed point located on Io's equator and in the sub-Jovian hemisphere.[1] The ground is supposed to be uniformly covered by the frost of SO_2 and the atmosphere to be a binary mixture composed of the vapor of the frost (i.e., SO_2 gas) and another noncondensable gas (SO or O_2).[2] When the eclipse begins, the temperature of the surface frost drops as a result of the loss of insolation and SO_2 condenses on the surface. Conversely, after the eclipse ends, the restored insolation raises the surface temperature and sublimation occurs. The condensation and sublimation on the surface induces an unsteady vertical motion of the overlying atmosphere. The presence of other components, S and O, is also well-known (Ballester et al., 1987). These components were assumed to stick to the surface in the previous simulations (e.g. Wong and Smyth, 2000) and were found to have only low concentration on the dayside of Io in the recent DSMC study by Walker (2012). In such a case, those components should not alter the results in this study significantly.

In the present study, we investigate the one-dimensional unsteady behavior during and after eclipse on the basis of kinetic theory. The basic assumptions are as follows: (i) the behavior of the atmosphere is described by the model Boltzmann equation for mixtures proposed in Andries et al. (2002); (ii) the vapor (SO_2 gas) follows the complete-condensation boundary condition on the surface [see Eqs. (6a) and (6b) appearing later]; (iii) the noncondensable gas (SO or O_2) follows the diffuse-reflection boundary condition on the surface. Note that the Boltzmann equation applies in this problem, since the local mean free path is not negligible compared to the pressure scale height during eclipse as well as at high altitudes [see Table 2 and Sections 3 and 4 appearing later]. Some additional assumptions, including those about the initial condition, will also be made in the course of the study.

In the following formulation, the vapor (SO_2 gas) and noncondensable gas (SO or O_2) will be referred to as species A and B, respectively. The Greek letters α and β will often be used to represent the species, i.e., $\alpha, \beta = \{A, B\}$. Let t be the time, where the eclipse begins at $t = 0$ and lasts until $t = 120$ min. Let $\boldsymbol{X}$ $[= (X_1, X_2, X_3)]$ be the space rectangular coordinates, where the surface is located at $X_1 = 0$ and the atmosphere extends over the half space $X_1 > 0$. The velocity distribution function (VDF) of molecules of species α $(= \{A, B\})$ is denoted as $F^\alpha = F^\alpha(t, X_1, \boldsymbol{\xi})$, where $\boldsymbol{\xi}$ $[= (\xi_1, \xi_2, \xi_3)]$ is the molecular velocity. The macroscopic quantities, such as the number density n^α, flow velocity $\boldsymbol{v}^\alpha$ $[= (v_1^\alpha, v_2^\alpha, v_3^\alpha)]$, pressure p^α, and temperature T^α of species α, are defined as the moments of F^α as follows:

$$n^\alpha = \int F^\alpha \mathrm{d}\boldsymbol{\xi}, \qquad \boldsymbol{v}^\alpha = \frac{1}{n^\alpha} \int \boldsymbol{\xi} F^\alpha \mathrm{d}\boldsymbol{\xi}, \tag{1a}$$

$$p^\alpha = k n^\alpha T^\alpha = \frac{1}{3} \int m^\alpha |\boldsymbol{\xi} - \boldsymbol{v}^\alpha|^2 F^\alpha \mathrm{d}\boldsymbol{\xi}, \tag{1b}$$

[1] As a result of tidal locking, Io always shows the same side (the sub-Jovian hemisphere) to Jupiter. Thus, the eclipse does not much effect the anti-Jovian hemisphere.

[2] Note that SO has not been established as a perfectly noncondensable gas in Io's circumstances. The effect of its partial condensation was examined in Moore et al. (2009).

where m^α is the molecular mass of species α, k is the Boltzmann constant, and $\mathrm{d}\boldsymbol{\xi} = \mathrm{d}\xi_1\mathrm{d}\xi_2\mathrm{d}\xi_3$. The domain of integration is the whole space of $\boldsymbol{\xi}$. The corresponding quantities of the total mixture, i.e., the number density n, flow velocity $\boldsymbol{v}$ [$= (v_1, v_2, v_3)$], pressure p, and temperature T of the mixture, are given by

$$n = \sum_{\alpha=A,B} n^\alpha, \tag{2a}$$

$$\boldsymbol{v} = \sum_{\alpha=A,B} m^\alpha n^\alpha \boldsymbol{v}^\alpha \Big/ \sum_{\alpha=A,B} m^\alpha n^\alpha, \tag{2b}$$

$$p = knT = \sum_{\alpha=A,B} \big(p^\alpha + \frac{1}{3} m^\alpha n^\alpha |\boldsymbol{v}^\alpha - \boldsymbol{v}|^2\big). \tag{2c}$$

In the present study, lateral winds are assumed to be small, so that the horizontal components of the flow velocity will be ignored (i.e., $v_2^\alpha = v_2 = 0$ and $v_3^\alpha = v_3 = 0$) in the actual analysis, whereas they are left in the formulation. This assumption may be unacceptable near the terminator, where supersonic horizontal flows have been found in the previous work (see, e.g., Ingersoll et al., 1985; Austin and Goldstein, 2000).

2.2. Basic equation and initial and boundary conditions

The model Boltzmann equation in Andries et al. (2002) for the present one-dimensional unsteady problem may be written in the following form. For $\alpha = \{A, B\}$,

$$\frac{\partial F^\alpha}{\partial t} + \xi_1 \frac{\partial F^\alpha}{\partial X_1} - g \frac{\partial F^\alpha}{\partial \xi_1} = K^\alpha (M^\alpha - F^\alpha), \tag{3}$$

where g is the gravitational acceleration. Since the scale height of the atmosphere is much smaller than the radius of Io, g ($= 1.8$ m/s^2) is treated as constant in the following analysis. The K^α and M^α are defined by

$$K^\alpha = \sum_{\beta=A,B} K^{\beta\alpha} n^\beta, \tag{4a}$$

$$M^\alpha = n^\alpha \Big(\frac{m^\alpha}{2\pi k T^{(\alpha)}}\Big)^{3/2} \exp\Big(-\frac{m^\alpha |\boldsymbol{\xi} - \boldsymbol{v}^{(\alpha)}|^2}{2kT^{(\alpha)}}\Big). \tag{4b}$$

Here, $K^{\beta\alpha}$ is a positive constant satisfying $K^{\beta\alpha} = K^{\alpha\beta}$, that determines the collision frequency of an α-species molecule with β-species molecules via $K^{\beta\alpha} n^\beta$. Thus, the above K^α corresponds to the total collision frequency of an α molecule. The parameters $\boldsymbol{v}^{(\alpha)}$ and $T^{(\alpha)}$ contained in the Maxwell distribution (4b) are defined by

$$\boldsymbol{v}^{(\alpha)} = \boldsymbol{v}^\alpha + \frac{2}{m^\alpha K^\alpha} \sum_{\beta=A,B} \mu^{\beta\alpha} X^{\beta\alpha} n^\beta (\boldsymbol{v}^\beta - \boldsymbol{v}^\alpha), \tag{5a}$$

$$\begin{aligned} T^{(\alpha)} = T^\alpha &- \frac{m^\alpha}{3k} |\boldsymbol{v}^{(\alpha)} - \boldsymbol{v}^\alpha|^2 \\ &+ \frac{4}{K^\alpha} \sum_{\beta=A,B} \frac{\mu^{\beta\alpha} X^{\beta\alpha} n^\beta}{m^\beta + m^\alpha} \Big(T^\beta - T^\alpha \\ &\qquad + \frac{m^\beta}{3k} |\boldsymbol{v}^\beta - \boldsymbol{v}^\alpha|^2\Big), \end{aligned} \tag{5b}$$

$$\mu^{\beta\alpha} = m^\beta m^\alpha / (m^\beta + m^\alpha). \tag{5c}$$

Note that n^α, $\boldsymbol{v}^\alpha$, and T^α appearing in the above equations are given by Eq. (1). That is, the model equation (3) is completed by Eq. (1) as well as Eqs. (4) and (5). Note also that $v_2^{(\alpha)} = v_3^{(\alpha)} = 0$ because of the assumption made after Eq. (2). The $X^{\beta\alpha}$ is an additional positive constant satisfying $X^{\beta\alpha} = X^{\alpha\beta}$; the positivity of $T^{(\alpha)}$ follows if $X^{\beta\alpha} \le K^{\beta\alpha}$. This model was designed in such a way that, by adjusting $X^{\beta\alpha}$, the momentum and energy exchanges between different species can be the same as those for (pseudo-)Maxwell molecules with an arbitrary value of the angular cutoff parameter.[3] For simplicity, in the present study we choose $X^{\beta\alpha}$ as specified in Eq. (14) below, so pseudo-Maxwell behavior of the molecules is not enforced.

The boundary condition on the surface is written as follows. For $X_1 = 0$ and $\xi_1 > 0$,

$$F^\alpha = n_w^\alpha \Big(\frac{m^\alpha}{2\pi k T_w}\Big)^{3/2} \exp\Big(-\frac{m^\alpha |\boldsymbol{\xi}|^2}{2kT_w}\Big), \tag{6a}$$

$$n_w^A = p_w^A / kT_w, \tag{6b}$$

$$n_w^B = -\Big(\frac{2\pi m^B}{kT_w}\Big)^{1/2} \int_{\xi_1<0} \xi_1 F^B \mathrm{d}\boldsymbol{\xi}. \tag{6c}$$

Here T_w is the surface temperature and varies with time as a result of the change of insolation. The p_w^A is the saturated vapor pressure at temperature T_w and is given by the Clausius–Clapeyron relation:

$$p_w^A = \Pi \exp(-\Gamma / T_w). \tag{7}$$

The Π and Γ are constants; $\Pi = 1.516 \times 10^{13}$ Pa and $\Gamma = 4510$ K for SO_2 vapor (Wagman, 1979). In the present problem, the variation of T_w and corresponding p_w^A with time would induce the unsteady motion of the atmosphere through the boundary condition (6). We will discuss how the surface temperature T_w is determined as a function of time t in the next section.

The initial condition is given as follows. The atmosphere at $t = 0$ is assumed to be in a saturated equilibrium state at rest with uniform temperature, i.e.,

$$F^\alpha = n_0^\alpha \Big(\frac{m^\alpha}{2\pi k T_0}\Big)^{3/2} \exp\Big(-\frac{m^\alpha (|\boldsymbol{\xi}|^2 + 2gX_1)}{2kT_0}\Big). \tag{8}$$

The initial temperature T_0 will be chosen in the next section. The n_0^α is the initial number density of species α on the surface ($X_1 = 0$); $n_0^A = p_0^A / kT_0$ with p_0^A being the saturated vapor pressure at temperature T_0 [i.e., p_0^A is given by Eq. (7) with T_w being replaced by T_0]. For later convenience, we introduce the concentration χ^B of the noncondensable gas contained in the initial atmospheric column,

[3] When an intermolecular force extending to infinity is considered, an angular cutoff is often introduced by ignoring a portion of grazing collisions to produce a finite collision frequency. See, e.g., Sone (2007) for more details.

which is defined as

$$\chi^B = \int_0^\infty n^B(t=0)\mathrm{d}X_1 \Big/ \int_0^\infty n(t=0)\mathrm{d}X_1$$
$$= \frac{(n_0^B/m^B)}{(n_0^A/m^A)+(n_0^B/m^B)}. \quad (9)$$

The above χ^B, instead of n_0^B, will be used later to specify the amount of the noncondensable gas.

2.3. Model for surface temperature

The surface temperature T_w is determined by the same differential equation as that in Moore et al. (2009), which may be written as

$$\frac{\mathrm{d}T_w}{\mathrm{d}t} = \begin{cases} A\sigma(T_{\mathrm{Min}}^4 - T_w^4), & \text{for } 0 \le t \le 120 \text{ min}, \\ A\sigma(T_{\mathrm{E}}^4 - T_w^4), & \text{for } t > 120 \text{ min}, \end{cases} \quad (10)$$

where σ is the Stefan–Boltzmann constant and $A = \varepsilon/C$ with ε being the bolometric emissivity and C the heat capacity per unit area of the surface. The T_{E} is an equilibrium temperature defined as

$$T_{\mathrm{E}} = \begin{cases} (T_{\mathrm{Max}} - T_{\mathrm{Min}})\cos^{1/4}\theta + T_{\mathrm{Min}}, \\ \qquad\qquad\qquad \text{for } \theta \le 90^\circ, \\ T_{\mathrm{Min}}, \qquad\quad \text{for } \theta > 90^\circ, \end{cases} \quad (11)$$

where θ is the solar zenith angle (SZA), T_{Max} is the maximum of T_{E} at the sub-solar point ($\theta = 0^\circ$), and T_{Min} is the minimum of T_{E} in the nightside hemisphere ($\theta > 90^\circ$). Note that T_{E} is a function of time t in the present problem, because θ at a fixed point on Io varies with time according to the diurnal motion of the sun. Once we specify the location (or the longitude) of the atmospheric column on the equator, we can determine the SZA as a function of t. The initial temperature T_0 appearing in Eq. (8) is then chosen as $T_0 = T_{\mathrm{E}}(t=0)$. The location of the column and values of A, T_{Max}, and T_{Min} will be specified in the next section.

In the above model for the surface temperature T_w, the effects of the latent heat of the phase transition and the sensible heat flowing through the interface are ignored. Those effects may be considered small, since the atmosphere is very thin (see the values of the saturated vapor pressure in Table 2 appearing later). However, one may consider that the effects of other heat sources (such as geothermal) which are practically time-independent are included in the minimum temperature T_{Min}. In any case, T_w in the above model is independent of the atmospheric behavior. We can solve Eq. (10) with the initial condition $T_w(t=0) = T_0$ to obtain T_w beforehand.

2.4. Parameter setting

In the present study, the minimum and maximum of the equilibrium temperature appearing in Eq. (11) are set as $T_{\mathrm{Min}} = 90$ K and $T_{\mathrm{Max}} = 114$ K, respectively. The location of the atmospheric column is set to the point with longitude 53°W, where the eclipse begins about 3 hours after sunrise and ends about 5 hours before noon. The initial SZA is $\theta(t=0) = 61^\circ$ and the initial temperature is then computed as $T_0 = 110$ K from Eq. (11). The species of the noncondensable gas, the initial concentration χ^B, and the parameter A appearing in Eq. (10) for the simulation cases considered in the present study are listed in Table 1.

Table 1: Parameter setting.

Case	gas B	m^B/m^A	χ^B	A^{-1}(J/m^{2}K)
1	—	—	0	350
2	SO	0.75	0.35	350
3	SO	0.75	0.35	700
4	SO	0.75	0.35	175
5	O_2	0.5	0.35	350
6	O_2	0.5	0.07	350

The above values of T_{Min} and A are quoted from the previous DSMC analysis in Moore et al. (2009), whereas the value of T_{Max} is lower than that in the same reference [$T_{\mathrm{Max}} = 120$ K in Moore et al. (2009)]. The lower T_{Max} is chosen to reduce the computational labor; a slight increase in the surface temperature results in considerably higher atmospheric pressure on the surface (see the saturated vapor pressure in Table 2 below). The numerical analysis of the Boltzmann equation generally becomes more difficult as the pressure increases. Incidentally, various values for T_{Min} and T_{Max} have been employed in the literature (see, e.g., Ingersoll et al., 1985; Smyth and Wong, 2004; Austin and Goldstein, 2000; Moore et al., 2009). The point with longitude 53°W is chosen so that the initial temperature T_0 coincides with those of the major results in Moore et al. (2009).

Next we choose values of the constants $K^{\beta\alpha}$ and $X^{\beta\alpha}$ appearing in the model Boltzmann equation (3). As mentioned after Eq. (4), $K^{\beta\alpha}$ is relevant to the molecular collision frequency. The mean free path ℓ_0 of SO_2 molecules with respect to collisions with other SO_2 molecules in the saturated equilibrium state with temperature T_0 may be defined as

$$\ell_0 = \frac{(8kT_0/\pi m^A)^{1/2}}{K^{AA}n_0^A}. \quad (12)$$

Then we assume that K^{AA} is determined so that the above ℓ_0 is equal to the mean free path of hard-sphere molecules with diameter d, i.e.,

$$\frac{(8kT_0/\pi m^A)^{1/2}}{K^{AA}n_0^A} = \frac{1}{\sqrt{2}\pi d^2 n_0^A},$$
$$\text{or} \quad K^{AA} = 4d^2(\pi kT_0/m^A)^{1/2}. \quad (13)$$

Here we substitute the nominal diameter of an SO_2 molecule $d = 7.16 \times 10^{-10}$ m. For the sake of simplicity, the other

Table 2: The saturated vapor pressure p_w^A, pressure scale height H^A, and molecular thermal speed c^A of SO_2 gas corresponding to temperature T_w. The mean free path ℓ_w (with respect to SO_2–SO_2 collisions) in the saturated equilibrium state with temperature T_w and the Knudsen number Kn are also shown. See Eqs. (7) and (15) [K^{AA} in Eq. (15b) is defined by Eq. (13) at $T_0 = 110$ K].

T_w(K)	p_w^A(Pa)	H^A(km)	c^A(m/s)	H^A/c^A(s)	ℓ_w(km)	Kn
90	2.62(−9)[a]	6.5	153	42	189	29
95	3.66(−8)	6.9	157	44	14.6	2.1
100	3.93(−7)	7.2	161	45	1.47	2.0(−1)
105	3.36(−6)	7.6	165	46	1.85(−1)	2.4(−2)
110	2.37(−5)	7.9	169	47	2.81(−2)	3.5(−3)
114	9.99(−5)	8.2	172	48	7.04(−3)	8.6(−4)

[a] Read as 2.62×10^{-9}.

constants K^{BB}, K^{BA}, and X^{BA} are all assumed to be identical with K^{AA}, i.e.,

$$\frac{K^{BB}}{K^{AA}} = \frac{K^{BA}}{K^{AA}} = \frac{X^{BA}}{K^{AA}} = 1. \tag{14}$$

We should note that the constants $K^{\beta\alpha}$ and $X^{\beta\alpha}$ are related to the properties of collisional interactions between molecules (as mentioned in Section 2.2) and also appear in the expressions of the transport coefficients, such as the viscosity, thermal conductivity, and diffusion coefficient (see Andries et al., 2002). Irrespective of values of $K^{\beta\alpha}$ and $X^{\beta\alpha}$, however, the model Boltzmann equation generally cannot match all the transport coefficients simultaneously.[4] The $K^{\beta\alpha}$ and $X^{\beta\alpha}$ determined above by Eqs. (13) and (14) will reproduce at least a proper value of the mean free path with respect to A–A collisions [or the Knudsen number defined by Eq. (15b) below], but will not yield totally correct transport properties of the mixture.

Figure 1 shows the variation of the surface temperature T_w during and after eclipse for different A's obtained as a solution of Eq. (10) with $T_{\rm Min}$, $T_{\rm Max}$, and T_0 specified above. As A^{-1} ($\sim$ the heat capacity per unit area of the surface) decreases, T_w changes more rapidly with a change of the insolation. Table 2 shows the saturated vapor pressure p_w^A corresponding to several T_w's in the temperature range in Fig. 1. In addition, the pressure scale height H^A and the molecular thermal speed c^A of species A, the mean free path ℓ_w with respect to A–A collisions in the saturated equilibrium state with temperature T_w, and the Knudsen number Kn, which indicates the degree of rarefaction, are also listed in the same table. Those are defined by

$$H^A = kT_w/m^A g, \quad c^A = (2kT_w/m^A)^{1/2}, \tag{15a}$$

$$\ell_w = (8kT_w/\pi m^A)^{1/2}/K^{AA} n_w^A, \quad \mathrm{Kn} = \ell_w/H^A. \tag{15b}$$

It is seen that p_w^A (and also ℓ_w) varies significantly in the above temperature range, whereas H^A and c^A show relatively small variations.

[4] The similar well-known example is the BGK model Boltzmann equation for a single-component gas (Bhatnagar et al., 1954; Welander, 1954), which always gives the Prandtl number Pr = 1.

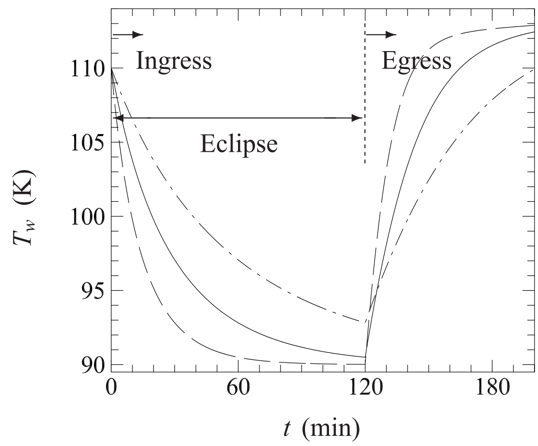

Figure 1: Surface temperature T_w during and after eclipse at the longitude of 53°W for $(T_{\rm Min}, T_{\rm Max}, T_0) = (90\ \mathrm{K}, 114\ \mathrm{K}, 110\ \mathrm{K})$. The solid line indicates the result for $A^{-1} = 350$ J/m^{2}K, the dashed line that for 175 J/m^{2}K, and the dot-dashed line that for 700 J/m^{2}K.

2.5. Numerical analysis

Suppose that the surface temperature T_w has been computed beforehand and given as a function of time t as shown in Fig. 1. Then we solve the initial-boundary value problem for the atmosphere, i.e., Eqs. (3), (6), and (8), numerically by means of a finite-difference method. The details of the method are omitted here, since we just follow a standard procedure; however its outline is given in Appendix A. The computational conditions, such as the grid intervals, time step, etc., as well as data concerning the accuracy are given in Appendix B.

In the following, the results in the case of pure SO_2 (Case 1 in Table 1) and in the case of a mixture (Case 2) are shown separately in Sections 3 and 4. The variation of the column density during eclipse and the comparison with the previous DSMC results are shown in Section 5.

3. Unsteady behavior of a pure SO_2 atmosphere

Figures 2–6 show the results for Case 1 in Table 1, i.e., the case of a pure SO_2 atmosphere.

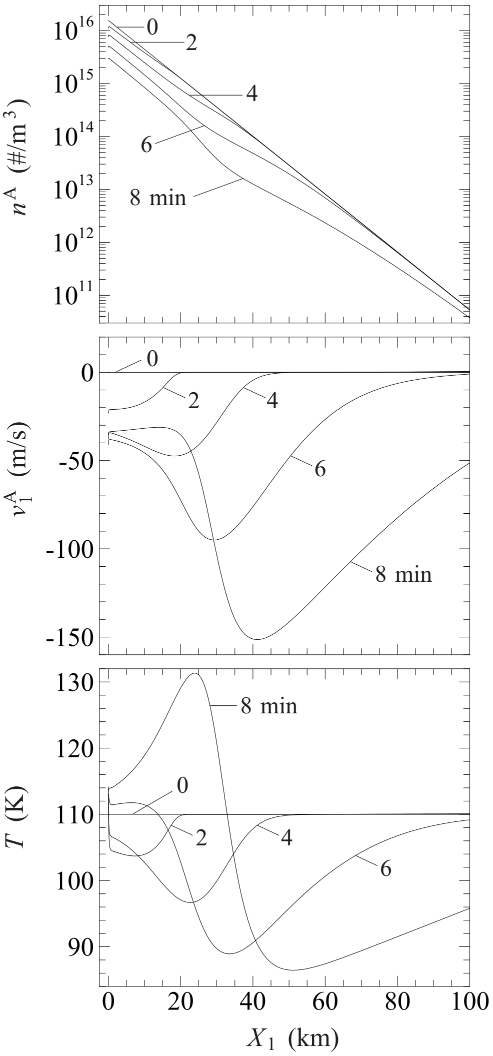

Figure 2: Profiles of the number density n^A, flow velocity v_1^A, and temperature T just after ingress into eclipse (t = 0, 2, 4, 6, and 8 min) in Case 1 [SO_2 (100%)].

3.1. During eclipse

Figure 2 shows the unsteady behavior of the atmosphere at the beginning of eclipse (the first 8 minutes after ingress into eclipse). The surface temperature T_w decreases to 104.8 K at $t = 8$ min (from the initial temperature 110 K). Thus, the saturation vapor pressure decreases, and the atmosphere starts condensing causing a sudden decrease of the density on the surface. As seen in the profile of n^A, the density decrease on the surface propagates upward as an expansion wave, which travels at the sound speed ($\sim$ 9.3 km/min) up to $t = 4$ min. After that, the wave front seems to accelerate. The local mean free path ℓ in the initial atmosphere is $\ell \sim 30$ m on the surface and increases about 10 times every 20 km (i.e., $\ell \sim 30$ km at 60 km height). Thus the upper atmosphere is practically a free-molecular gas, so that its density profile is affected by the ballistic motion of fast molecules.

As seen in the profile of v_1^A, the condensation on the surface induces a downward flow. However, when $t \gtrsim 4$ min, the maximum flow speed is achieved not on the surface but at intermediate altitudes. This indicates that the high speed flow *falling* from the upper atmosphere collides with the lower atmosphere and is decelerated near the surface. In this process, the atmosphere is compressed, so that the temperature rises significantly (cf. the profile of T). Then the compressed region propagates upward, as a collisional shock wave, against the high speed downward flow; when $t = 8$ min, the local mean free path is about 2 km at $X_1 = 20$ km, 10 km at $X_1 = 30$ km, and 30 km at $X_1 = 40$ km. We note here that the temperature of the gas adjacent to the surface is higher than the surface temperature (e.g., $T = 113.5$ K at $X_1 = 0$ km and $t = 8$ min). The mechanism of this temperature rise on the condensing

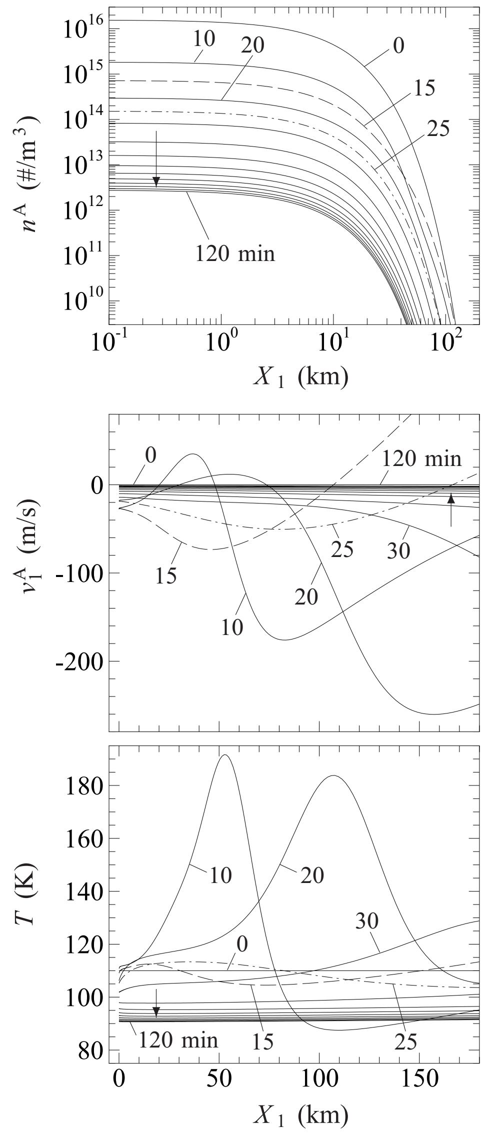

Figure 3: Profiles of the number density n^A, flow velocity v_1^A, and temperature T during eclipse in Case 1 [SO_2 (100%)]. The solid lines show the profiles at every 10 minutes (t = 0, 10, 20, . . ., 120 min); the dashed and dashed-dotted lines show the profiles at t = 15 and 25 min. The arrow indicates the direction to which the profile moves with time ($t \gtrsim 30$ min).

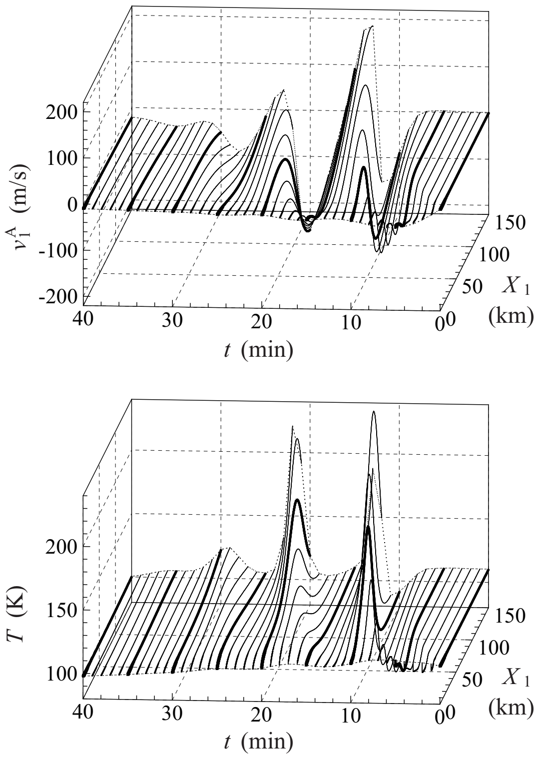

Figure 4: Profiles of the flow velocity v_1^A and temperature T at every minute until t = 40 min in Case 1 [SO_2 (100%)]. The thick lines indicate the profiles at every 5 minutes.

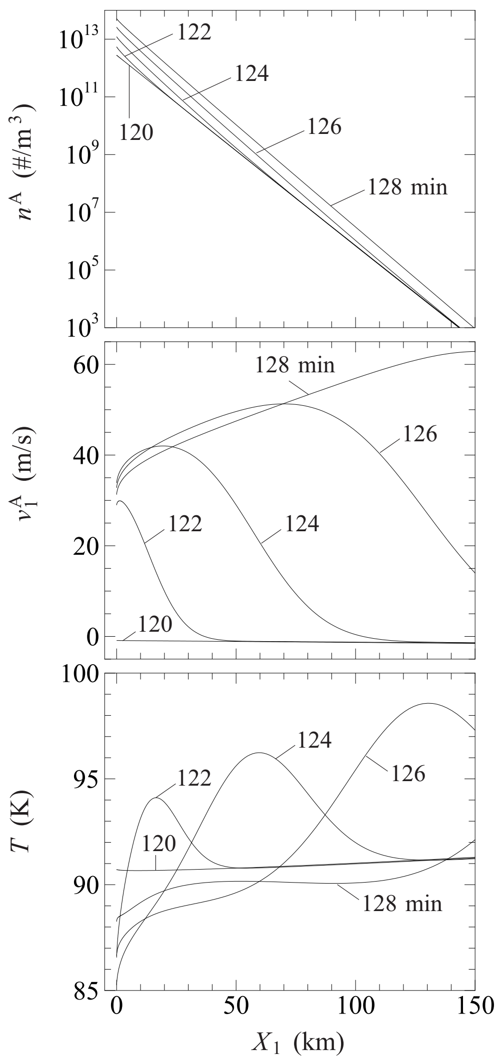

Figure 5: Profiles of the number density n^A, flow velocity v_1^A, and temperature T just after egress (t = 120, 122, 124, 126, and 128 min) in Case 1 [SO_2 (100%)].

surface and that of the temperature drop on the evaporating (or sublimating) surface appearing later were clarified and explained physically by Sone and Onishi (1978) (see also Sone, 2002).

Figure 3 shows the time evolution of the profiles during the rest of the eclipse (i.e., $t = 0 - 120$ min). The number density continues to decrease at lower altitudes because of the condensation on the surface, whereas the profile at higher altitudes shows oscillatory behavior until $t \sim 30$ min. The flow velocity profile shows that there is a layer moving upward (i.e., with positive flow velocity) at $t = 10$ min. The positive peak of the profile has developed from the maximum seen at $t = 8$ min around $X_1 = 20$ km (see Fig. 2). This is due to the fact that a part of the gas flowing down at a high speed from the upper atmosphere is bounced upward when colliding with the lower and denser atmosphere. The temperature there increases up to about 190 K. These peaks in the flow velocity and temperature profiles at $t = 10$ min develop further and move upward at a high speed (5 or 6 times the sound speed). However, the rising layer finally loses energy and starts falling again. The falling gas is bounced upward again, causing the second rising layer, which can be observed in the flow velocity profile at $t = 20$ min. This process is repeated once again. As a result, the flow velocity and temperature at a fixed altitude oscillate in time, while the amplitude decays rapidly and almost vanishes by $t \sim 40$ min. The time evolution of the flow velocity and temperature profiles during this process is shown in Fig. 4, from which the oscillatory behavior is seen more clearly. After the oscillation ceases, the flow speed and the temperature decrease uniformly at all altitudes until the end of the eclipse. At t =120 min, the density on the surface decreases to be $O(10^{-4})$ times smaller than its initial value and the local mean free path at the surface extends to as much as 145 km.

3.2. After eclipse

Figure 5 shows the unsteady behavior during the first 8 minutes after egress. The surface temperature T_w, which decreased to 90.5 K at t = 120 min, starts rising and becomes 96.8 K at t = 128 min. Then the saturation vapor pressure increases and the sublimation begins on the surface. Since the whole atmosphere is almost free-molecular gas at this time, the molecules emitted from the surface fly ballistically and convey the disturbances due to the change of T_w directly to the upper atmosphere. As a result, the disturbances travel faster than the sound speed but do not

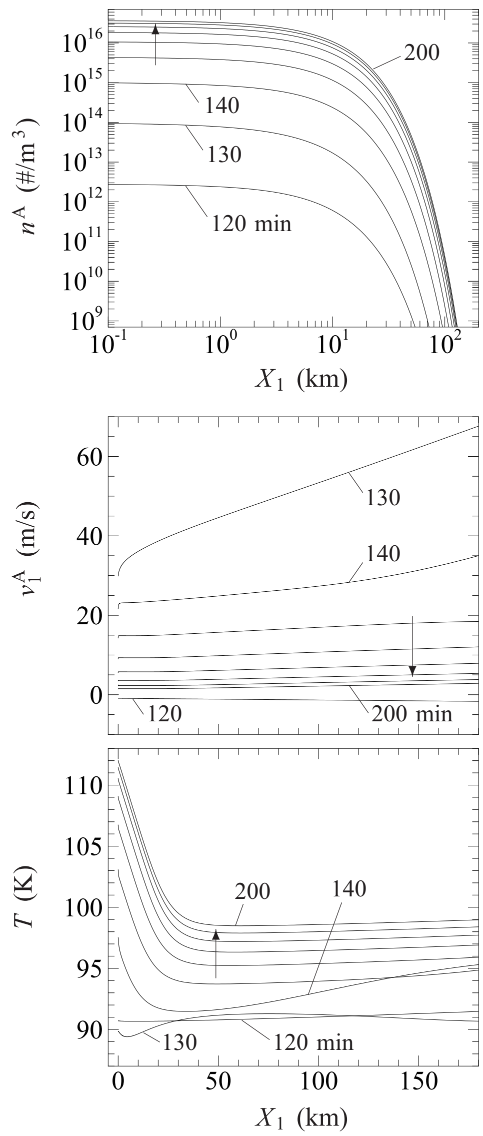

Figure 6: Profiles of the number density n^A, flow velocity v_1^A, and temperature T after eclipse ($t = 120, 130, 140, \ldots, 200$ min) in Case 1 [SO_2 (100%)]. See the caption of Fig. 3.

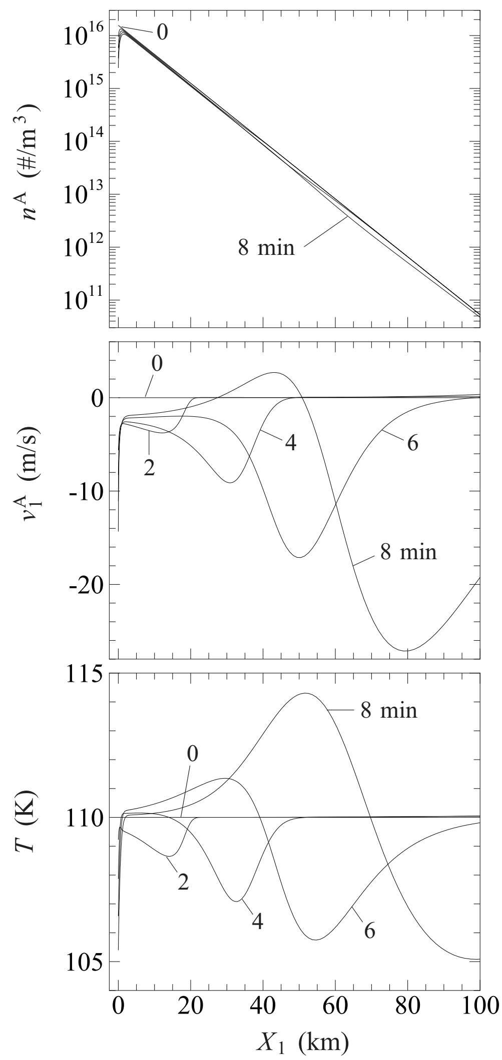

Figure 7: Profiles of the number density n^A of SO_2, flow velocity v_1^A of SO_2, and temperature T of the mixture just after ingress into eclipse ($t = 0$, 2, 4, 6, and 8 min) in Case 2 [SO_2 (65%) and SO (35%)].

form a collisional shock wave. Note again that the temperature drop phenomenon on the sublimating surface is clearly seen in the profile of T.

Figure 6 shows the profiles at every 10 minutes after the eclipse until $t = 200$ min. The number density increases rapidly and its initial value at $t = 0$ min near the surface (see Fig. 3) is restored at $t \sim 160 - 170$ min. The flow velocity increases during the first 10 minutes and then decreases uniformly. The gas temperature on the surface, which is at each time a bit lower than the surface temperature T_w because of the temperature drop phenomenon (e.g., $T_w = 112.4$ K at $t = 200$ min), rises continuously with time as T_w rises. Then, the temperature rise near the surface is propagated upward by the sublimating flow. The temperature profile for $t \gtrsim 150$ min becomes flat in the upper region $X_1 \gtrsim 50$ km. Incidentally, the local mean free path at $X_1 = 50$ km is about 100 km at $t = 150$ min and shrinks to 9 km at $t = 200$ min.

4. Unsteady behavior in the case of the mixture

Figures 7–12 show the results for Case 2 in Table 1, i.e., the case of the mixture of SO_2 (gas A) and SO (gas B). The surface temperature as a function of time is the same as that in Case 1. The concentration of SO in the initial atmospheric column is set as $\chi^B = 0.35$.

4.1. During eclipse

Figure 7 shows the behavior of the number density n^A of SO_2, flow velocity v_1^A of SO_2, and temperature T of the mixture at the beginning of eclipse (the first 8 minutes after ingress into eclipse). In comparison with the pure SO_2 case shown in Fig. 2, the number density decreases only slightly (except in the immediate vicinity of the surface)

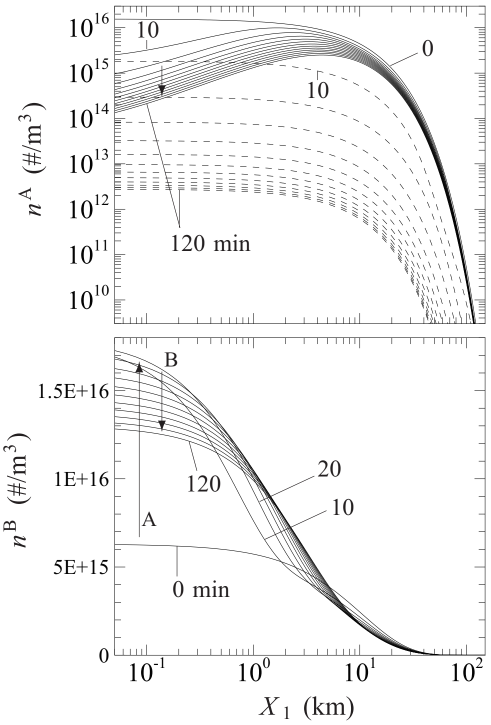

Figure 8: Profiles of the number densities n^A of SO_2 and n^B of SO during eclipse ($t = 0, 10, 20, \ldots, 120$ min) in Case 2 [SO_2 (65%) and SO (35%)]. The dashed lines in the upper panel indicate corresponding profiles in Case 1 [SO_2 (100%)] shown in Fig. 3. See the caption of Fig. 3. In the lower panel, Arrow A is for $t \leq 20$ min and B for the subsequent time.

and the condensing flow speed is small. Since the condensation is weak, the temperature rise phenomenon on the condensing surface is inconspicuous. Instead, the gas temperature near the surface follows the decreasing surface temperature and shows a steep gradient. The profiles of the flow velocity v_1^B of SO (not shown in the figure) are similar to those of v_1^A except near the surface; $v_1^B = 0$ on the surface because of the diffuse-reflection boundary condition for the noncondensable gas [see Eq. (6)].

Figure 8 shows the profiles of the number density n^A of SO_2 and n^B of SO at every 10 minutes during the eclipse. The corresponding profiles in the pure SO_2 case (shown in Fig. 3) are also plotted with dashed lines. The density of the noncondensable gas SO increases near the surface rapidly in the first 20 minutes (see Arrow A), since SO is carried by the downward condensing flow of SO_2 and accumulates there. The SO near the surface forms a diffusion layer, which interrupts the condensation of SO_2. Consequently the density of SO_2 decreases only at lower altitudes and the profile hardly changes at higher altitudes. Its value on the surface at the end of the eclipse is about $O(10^2)$ times larger than the corresponding value in the pure SO_2 case. In this way, the atmospheric collapse during the eclipse is interrupted by the noncondensable component. After the first 20 minutes the density of SO near the surface slowly decreases as a result of upward self-diffusion (see Arrow B). Incidentally, the local mean free path on the surface may be estimated at $\sim$30 m at the end of the eclipse.

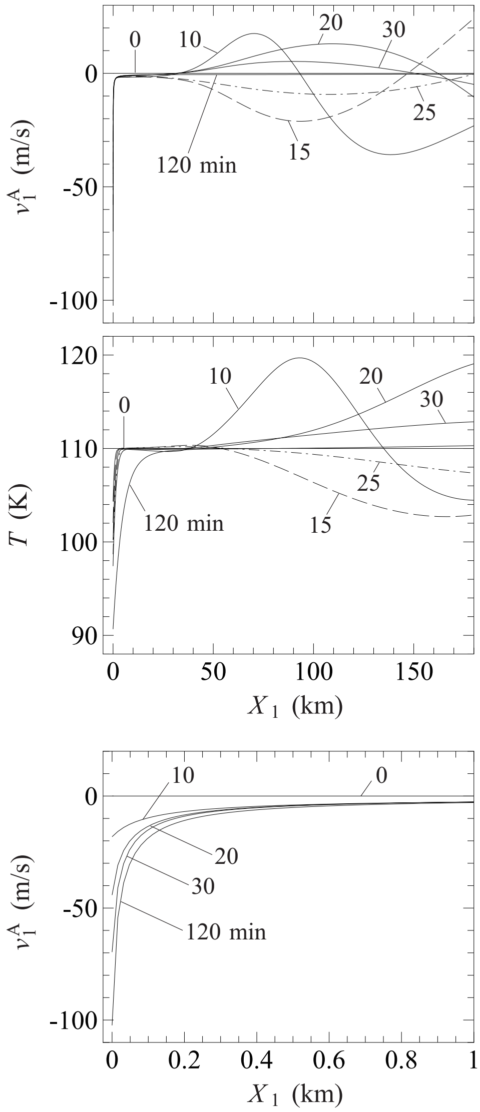

Figure 9: Profiles of the flow velocity v_1^A of SO_2 and temperature T of the mixture during eclipse in Case 2 [SO_2 (65%) and SO (35%)]. The solid lines show the profiles at $t = 0$, 10, 20, 30, and 120 min; the dashed and dashed-dotted lines in the upper two panels show the profiles at $t = 15$ and 25 min. The nethermost panel shows the magnified profile of v_1^A in the vicinity of the surface.

Figure 9 shows the flow velocity v_1^A of SO_2 and temperature T of the mixture during the eclipse. Because the SO layer constitutes a partial barrier against the condensation, the flow speed of SO_2 decreases quickly and almost vanishes at all altitudes except near the surface. A rapidly condensing flow remains in the close vicinity of the surface, since a large difference between the SO_2 number density near the surface and the saturation number density corresponding to the surface temperature is maintained until the end of the eclipse. The temperature field behaves quite differently compared with the pure SO_2 case shown in Fig. 3. Towards the end of the eclipse, the tem-

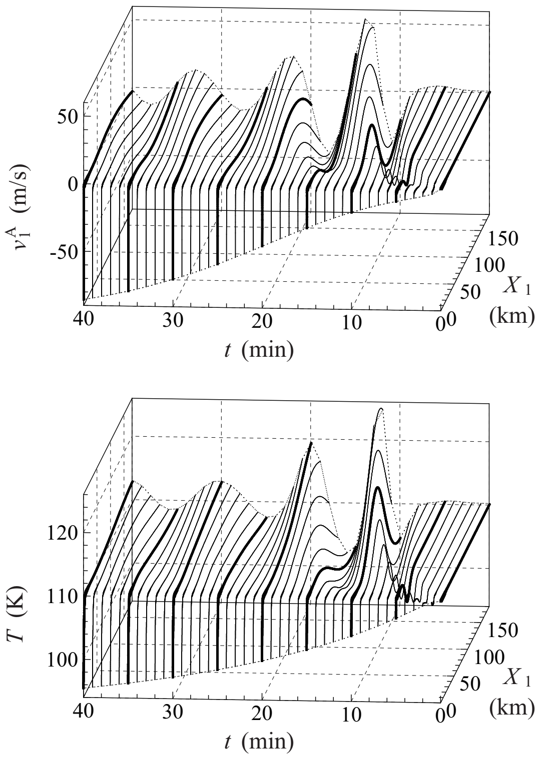

Figure 10: Profiles of the flow velocity v_1^A and temperature T at every minute until $t = 40$ min in Case 2 [SO_2 (65%) and SO (35%)]. See the caption of Fig. 4.

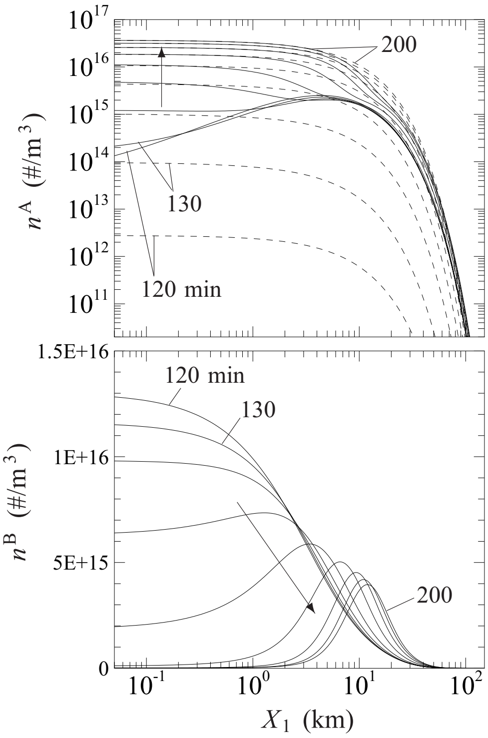

Figure 11: Profiles of the number densities n^A of SO_2 and n^B of SO after eclipse (t = 120, 130, 140, ..., 200 min) in Case 2 [SO_2 (65%) and SO (35%)]. The dashed lines in the upper panel indicate corresponding profiles in Case 1 [SO_2 (100%)] shown in Fig. 6. See the caption of Fig. 3.

perature returns to its initial value 110 K except near the surface, where the effect of surface temperature spreads by conduction.

As in the case of the pure SO_2 shown in Figs. 3 and 4, the flow velocity and temperature at a fixed altitude oscillate in time because of the same mechanism. This is seen from Fig. 9 and from Fig. 10 that corresponds to Fig. 4. For instance, in the former figure, one observes the first layer of SO_2 moving upward (with positive v_1^{A}) at $t = 10$ min and the second (thicker) layer at $t = 20$ min, as in Fig. 3. However, since the speed of falling of SO_2 caused by condensation is lower in the presence of the noncondensable SO, the oscillation is weaker and inconspicuous at lower altitudes ($X_1 \lesssim 40$ km). On the other hand, the oscillation lasts much longer than in the pure SO_2 case because the falling SO_2 is bounced upward more strongly by the dense layer of SO near the ground. The oscillation period measured from the result is about 10 minutes, whereas the Brunt–Väisälä period for the initial (isothermal) state for Case 2 computed by a textbook formula is about 11.5 minutes.

4.2. After eclipse

Figure 11 shows the SO_2 and SO number density profiles at every 10 minutes after egress until $t = 200$ min. Here again the corresponding profiles in the pure SO_2 case (shown in Fig. 6) are also plotted with dashed lines. The SO_2 density remains almost unchanged for a while just after egress. After the surface temperature and the corresponding saturation density rise sufficiently, however, sublimation of SO_2 takes place. As the result, the SO_2 density starts increasing and SO is lifted near the surface. In particular, the SO near the surface is swept away strongly during the $t \sim 140 - 170$ min period and then an SO-rich layer is formed around the altitude of 10 km. Correspondingly, a hollow is formed in the profile of SO_2 density at the same altitude.

Figure 12 shows the flow velocity of SO_2 and temperature of the mixture after egress until $t = 200$ min. Condensation, leading to a downward flow, continues for a while after egress. Then, sublimation, giving rise to an upward flow, follows at $t \sim 140 - 150$ min. The flow speed increases until $t \sim 170$ min and then decreases at all altitudes. Even at $t = 170$ min, however, the flow speed is small compared with the pure SO_2 case (see Fig. 6). The gas temperature near the surface rises immediately after egress following the increase of the surface temperature.

5. Column density and comparison with the previous DSMC result

The column density of SO_2 during and after eclipse is shown in Fig. 13(a) (cf. Table 1). In the case of the pure SO_2 atmosphere (Case 1), the column density at the end of the eclipse is almost 10^4 times smaller than its initial

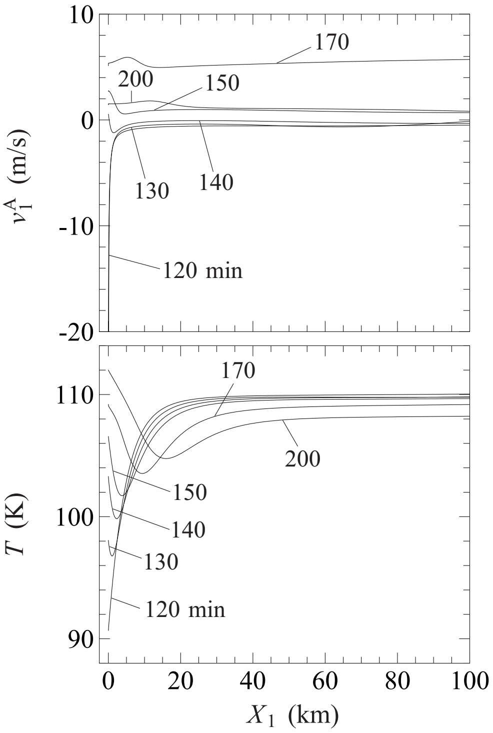

Figure 12: Profiles of the flow velocity v_1^A of SO_2 and temperature T of the mixture after eclipse ($t = 120$, 130, 140, 150, 170, and 200 min) in Case 2 [SO_2 (65%) and SO (35%)].

value. In the case of the mixture, the noncondensable gas interrupts the condensation of SO_2 and slows down the atmospheric collapse. Comparing the results of Cases 2 and 5, we see that the collapse is delayed more efficiently by heavier SO than by O_2, if the total amount (or χ^B) is fixed. Comparison of the results of Cases 5 and 6 naturally shows that a larger amount of the noncondensable gas (or larger χ^B) has a greater inhibiting effect on collapse during eclipse (for fixed m^B). However, it should be remarked that even a small amount of it ($\chi^B = 0.07$) affects the column density significantly (Aoki et al., 1998, 2003; Moore et al., 2009). When the heat capacity of the surface ($\sim A^{-1}$) is larger (Case 3) or smaller (Case 4), the temperature drop during the eclipse and rise after egress are slower or faster, respectively (see Fig. 1). Correspondingly, in comparison with Case 2, the increase of the column density after egress is slower in Case 3 and faster in Case 4. However, the difference in the heat capacity in Cases 2, 3, and 4 has virtually no effect on the columns during eclipse because the atmospheric collapse is so efficiently hindered. The dotted line in the figure indicates the theoretical value for the pure SO_2 atmosphere, which is at every moment in an isothermal saturated equilibrium state at rest (with $A^{-1} = 350$ J/m^{2}K). Since the actual atmosphere cannot equilibrate with the surface instantaneously, the result of Case 1 lags slightly behind the instantaneous equilibrium.

Now the column density shown in Fig. 13(a) is compared with the previous DSMC result, i.e., Fig. 8 in Moore et al. (2009). Figure 13(b) is its extracted reproduction based on the data provided by C. H. Moore, where their cases are indicated by the subscript M as (Case 1)$_{\mathrm{M}}$. Our Case 1 corresponds to (Case 1)$_{\mathrm{M}}$, Case 2 to (Case 5)$_{\mathrm{M}}$, Case 3 to (Case 7)$_{\mathrm{M}}$, Case 4 to (Case 8)$_{\mathrm{M}}$, Case 5 to (Case 3)$_{\mathrm{M}}$, and Case 6 to (Case 2)$_{\mathrm{M}}$ (cf. Table 1), but the parameters are not exactly the same; for instance, the initial SZA is 61° in our case and 78° in Moore et al. (2009). Figures 13(a) and 13(b) look similar, the main discrepancy being as follows: First in Case 6, where O_2 is a small fraction ($\chi^B = 0.07$), we obtain larger columns during eclipse (especially at the end of eclipse) compared to (Case 2)$_{\mathrm{M}}$; Secondly the result of Case 1 (pure SO_2 case) is closer to the dotted line (the analytical result for an isothermal equilibrium atmosphere) than the corresponding DSMC result [(Case 1)$_{\mathrm{M}}$]. We note that both discrepancies appear when χ^B is small. Apart from those discrepancies, the similarity between Figs. 13(a) and 13(b) indicates an agreement of the gross atmospheric collapse and reformation dynamics. Thus, as discussed in Moore et al. (2009), the present results are also consistent with the collapse time scale of 20 – 30 minutes observed via an auroral emission intensity during eclipse in Clarke et al. (1994) and Retherford et al. (2007).

Finally, the unsteady behavior of the atmosphere in Case 2, which has already appeared in Figs. 7–12, is shown again in Fig. 14; it is plotted in the same form as the corresponding figures in Moore et al. (2009) to facilitate the comparison. Panel (a) may be directly compared with Fig. 4(b) [or more appropriately with Fig. 6(a)] in Moore et al. (2009) and panel (b) with Fig. 10 in the same reference. In the DSMC simulations in Moore et al. (2009), the heating effect of the plasma torus was taken into account, so that a temperature rise is observed in the upper atmosphere. Instead, the present result is naturally almost isothermal. However, the profiles of the number densities n^{A} and n^{B} in Fig. 14 are quite similar to the DSMC result.

Apart from the neglect of the effect of plasma impingement, the use of the model Boltzmann equation and the choice for the values of its parameters $K^{\beta\alpha}$ and $X^{\beta\alpha}$ [see Eqs. (13) and (14)], which specify molecular properties, may also cause differences. The VHS molecular model was employed in the previous DSMC simulations, whereas the present simulations do not. Nevertheless, as we have seen above, our present approach reproduces, on the whole, the behavior obtained in Moore et al. (2009). Therefore, the more detailed time evolutions of the profiles presented in Figs. 2–12, which are practically impossible to obtain by the DSMC method, provide new and important information.

6. Concluding remarks

The unsteady behavior of Io's atmosphere during and after eclipse was studied on the basis of kinetic theory. Following the previous DSMC simulation in Moore et al. (2009), we considered the atmospheric column above a fixed point on Io's surface and analyzed the one-dimensional

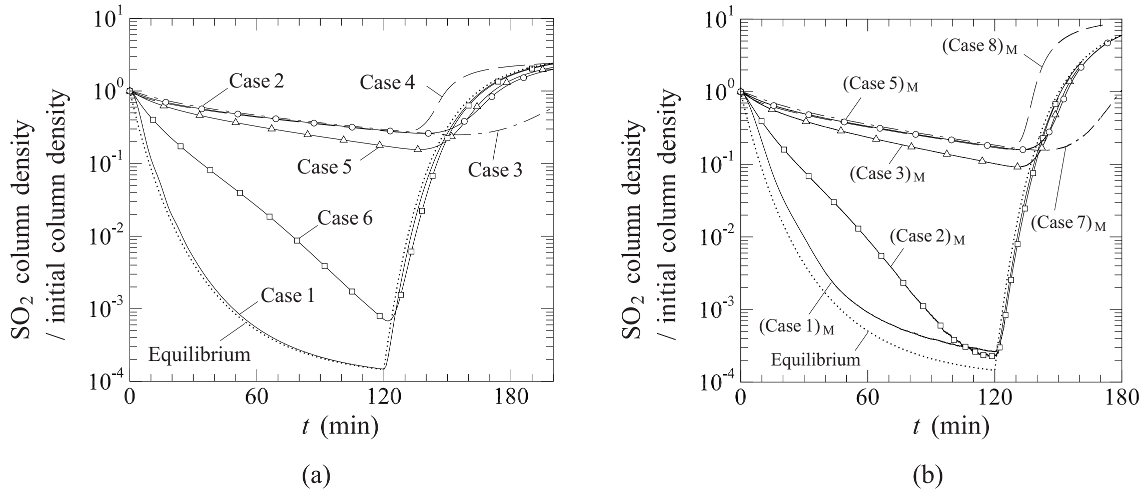

Figure 13: Normalized column density of SO_2. (a) Present results and (b) DSMC results in Moore et al. (2009). The initial column density is 1.2386×10^{20} $\#/\mathrm{m}^2$. The dotted line indicates the theoretical value for hypothetical pure SO_2 atmosphere in an isothermal saturated equilibrium state at rest when $A^{-1} = 350$ $\mathrm{J/m^2K}$.

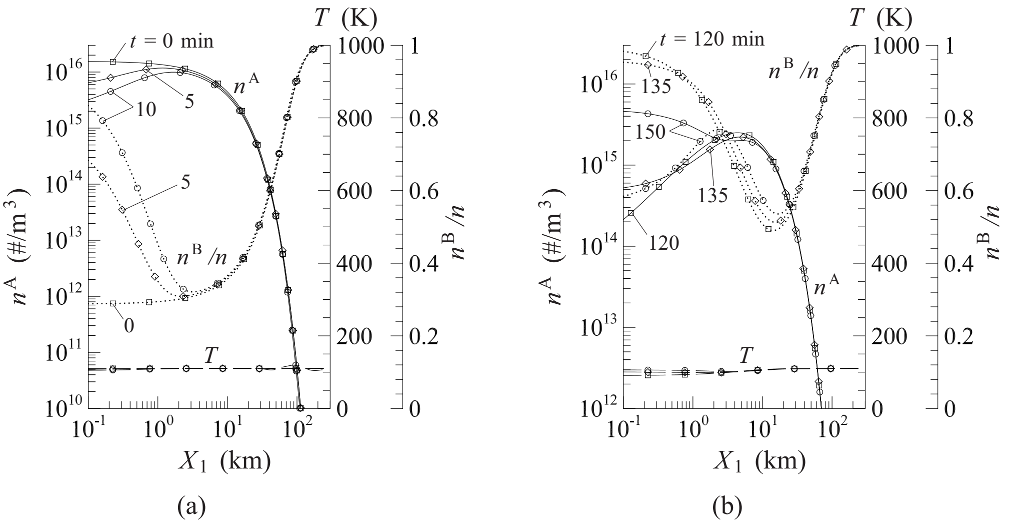

Figure 14: The behavior of the atmosphere in Case 2 (a) for the first 10 minutes after ingress and (b) for the first 30 minutes after egress. The solid lines indicate the number density n^A of SO_2, the dotted lines the concentration n^B/n of SO, and the dashed lines the temperature T of the mixture.

flow induced by condensation and sublimation of SO_2. In the present study, we focused on the effect of the noncondensable gas (SO or O_2) only and ignored other effects, such as the plasma impingement, radiative cooling of the gas, molecular internal structure, and reactions between the component species. Moreover, instead of the full Boltzmann equation, we used the model equation in Andries et al. (2002) for easy analysis. However, we carried out computations by means of a finite-difference method to obtain accurate results.

In spite of the simplifications mentioned above, the column density of SO_2 during eclipse almost coincides with the DSMC result, except for a few discrepancies. Thus, we may say that the atmospheric collapse and the interruption by a noncondensable gas are, as a whole, correctly reproduced in the present simulation. This is because, as expected, the effect of the noncondensable gas is the most dominant in this problem. As mentioned in Section 2.4, the model equation cannot yield totally correct transport properties of the mixture. However, this should not be a serious defect, because the present problem is controlled mainly by the effect of the mutual diffusion only.

The solutions obtained in the present approach may have some restrictions because of the simplifications. However, they were able to clarify some detailed structures, such as the waves in the macroscopic quantities traveling in the column and an oscillatory motion in the atmosphere during eclipse, that had not been noticed in Moore et al. (2009). Indeed, it is a formidable task to find such detailed structures of the atmospheric behavior by the DSMC simulation, especially in the case of unsteady problems. Therefore, we may emphasize that the present results provide a deeper understanding of the phenomena found in Moore et al. (2009) and thus complement this reference.

Acknowledgements

This work was partially supported by the Grants-in-Aid for Scientific Research, No. 21760129 from MEXT and No. 23246034 from JSPS.

Appendix A. Outline of numerical analysis

We first note that the molecular-velocity variables ξ_2 and ξ_3 can be eliminated from the problem by introducing appropriate marginal VDF's as in Chu (1965) (see also Sone, 2007, A.6). The initial-boundary value problem, Eqs. (3), (6), and (8), is then recast into a problem for the marginal VDF's depending only on t, X_1, and ξ_1, which is much easier to handle.

Next we limit the variables X_1 and ξ_1 to the finite range, say, $0 \leq X_1 \leq D$ and $|\xi_1| \leq Zc_0^\alpha$ for species α $(= \{A, B\})$ with sufficiently large D and Z. Here c_0^α is the molecular thermal speed of species α at temperature T_0 [i.e., the second equation of Eq. (15a) with T_w and m^A being replaced by T_0 and m^α, respectively]. The grid points $X^{(i)}$ $(i = 0, 1, \dots, M;\ X^{(0)} = 0;\ X^{(M)} = D)$ for X_1 are defined as

$$X^{(i)} = \begin{cases} -H_0^A \ln(1 - \epsilon i), & (i = 0, 1, \dots, \bar{M}), \\ P_{\bar{M}-2}(i) + P_{\bar{M}-1}(i) + P_{\bar{M}}(i), & \\ \qquad (i = \bar{M}+1, \bar{M}+2, \dots, M), & \end{cases} \tag{A.1}$$

where H_0^A is the scale height at temperature T_0 [i.e., the first equation of Eq. (15a) with T_w being replaced by T_0], ϵ is a sufficiently small constant, and

$$P_l(i) = X^{(l)} \frac{(i-m)(i-n)}{(l-m)(l-n)}, \tag{A.2}$$

with (l, m, n) being the permutation of $(\bar{M}-2, \bar{M}-1, \bar{M})$. The above $X^{(i)}$'s up to $i = \bar{M}$ are arranged so that the grid interval grows exponentially with altitude and can be comparable to the local mean free path; $X^{(i)}$'s for $i > \bar{M}$ are arranged in such a way that the growth rate of the interval is reduced to have sufficient number of grid points at higher altitudes and be smoothly connected at $i = \bar{M}$. The grid points $\xi_\alpha^{(j)}$ for species α $(j = -2N, -2N+1, \dots, 2N;\ \xi_\alpha^{(\pm 2N)} = \pm Zc_0^\alpha;\ \xi_\alpha^{(0)} = 0)$ for ξ_1 are defined as

$$\xi_\alpha^{(j)} = \begin{cases} Zc_0^\alpha (j/2N)^2, & (j \geq 0), \\ -\xi_\alpha^{(-j)}, & (j < 0). \end{cases} \tag{A.3}$$

In general, the extent of the VDF of species α in the molecular velocity space is inversely proportional to $\sqrt{m^\alpha}$ [see, e.g., Eq. (8)]. Thus $\xi_\alpha^{(j)}$'s for each species differ accordingly. The values of ϵ, $\bar{M}$, and M in Eq. (A.1) as well as those of Z and N in Eq. (A.3) are specified in Appendix B.

We employ an implicit finite-difference scheme for the equation of the marginal VDF's, which is essentially the same as that in Aoki et al. (1990) except that a derivative with respect to ξ_1 exists in the present problem; a standard (upwind) finite difference of 2nd-order accuracy (see, e.g., Ohwada et al., 1989, Appendix A) is used to express the derivatives with respect to X_1 and ξ_1. Note that the Boltzmann equation should be solved in accordance with the direction of the characteristics, which in the present problem are equivalent to the trajectories of a projectile in the phase space starting from $X_1 = 0$ with various initial velocities ξ_1 (> 0) [see Eq. (3)]. To be consistent with that direction, the finite-difference solution on the grid points should be constructed in the following manner: (i) the solution for $\xi_\alpha^{(j)} \geq 0$ is constructed successively from $X^{(1)}$ to $X^{(M)}$ and for each $X^{(i)}$ successively from $\xi_\alpha^{(2N-1)}$ to $\xi_\alpha^{(0)}$; (ii) the solution for $\xi_\alpha^{(j)} < 0$ is constructed successively from $X^{(M-1)}$ to $X^{(0)}$ and for each $X^{(i)}$ successively from $\xi_\alpha^{(-1)}$ to $\xi_\alpha^{(-2N)}$. In this procedure, auxiliary boundary conditions at $\xi_\alpha^{(2N)}$ and at $X^{(M)}$ for $\xi_\alpha^{(j)} < 0$ are necessary. Here we assume that $F^\alpha(\xi_\alpha^{(2N)}) = 0$, since $F^\alpha \to 0$ as $|\boldsymbol{\xi}| \to \infty$ in general. As for the condition at $X^{(M)}$ we assume the specular reflection, i.e., $F^\alpha(X^{(M)}, \xi_\alpha^{(j)}) = F^\alpha(X^{(M)}, -\xi_\alpha^{(j)})$ for $\xi_\alpha^{(j)} < 0$. As a result of the latter condition, the atmospheric escape (Jeans escape) is neglected in the present study [Note that the escape velocity on Io (about 2.56 km/s) is very fast compared to the typical thermal speed of molecules (see Table 2)].

Finally it should be mentioned that the derivative with respect to ξ_1 of the VDF on the surface $(X_1 = 0)$ may be discontinuous at $\xi_1 = 0$ in the present problem (the VDF itself is continuous). The discontinuity is properly taken into account in the above scheme.

Appendix B. Grid parameters and accuracy tests

The results shown in Sections 3–5 were obtained under the following computational conditions: (i) the time step was 4.694 ms; (ii) the parameters for $X^{(i)}$ in Eq. (A.1) were set as $(\epsilon, \bar{M}, M) = (0.002, 480, 616)$; (iii) the parameters for $\xi_\alpha^{(j)}$ in Eq. (A.3) were set as $(Z, N) = (6, 200)$. See Table 2 for the values of H_0^A and c_0^A at $T_0 = 110$ K. The extent of the spatial grids D was about 246 km and the minimum and maximum intervals were 15.9 m (on the surface) and 2.84 km (at $X_1 = D$). The computation, which was not parallelized, was mainly carried out on a personal computer with an Intel Core i7–870 (2.93GHz) processor and took approximately 60 hours for each case until $t = 300$ min.

We also carried out auxiliary runs for Cases 1 and 2 varying the computational condition as listed below. The macroscopic quantities obtained in those test runs were compared with the results shown in Sections 3 and 4.

(a) The time step was doubled (9.388 ms) without changing the above $X^{(i)}$'s and $\xi_\alpha^{(j)}$'s. The differences of n^α, T, and v_1^α (from the results shown in Sections 3 and 4) were, respectively, less than 0.12 %, 0.07 %, and 0.2 m/s (0.01 m/s for $t > 40$ min) at every point up to an altitude of 180 km.

(b) The number of ξ_1 grid points was reduced by setting $N = 160$. Up to an altitude of 150 km, the differences of n^α, T, and v_1^α were less than 8.4 %, 0.85 %, and 1.7 m/s (0.33 m/s for $t > 40$ min) in Case 1. Up to an altitude of 180 km, they were less than 12 %, 0.92 %, and 4.6 m/s (0.41 m/s for $t > 40$ min) in Case 1 and less than 4.3 %, 0.24 %, and 1.5 m/s (0.11 m/s for $t > 40$ min) in Case 2.

(c) The number of X_1 grid points were reduced by taking only even-numbered points from the above $X^{(i)}$'s (i.e., $X^{(2i)}$ with $i = 0, 1, \ldots, M/2$). In Case 1, the differences of n^A, T, and v_1^A for $t \le 40$ min were less than 2.6 %, 2.3 %, and 2.6 m/s (or 15 %, 7 %, and 22.6 m/s) up to an altitude of 150 km (or 180 km) and those for $t > 40$ min were less than 2.3 %, 0.24 %, and 0.83 m/s up to an altitude of 180 km. In Case 2, the differences of n^α, T, and v_1^α were less than 5.2 %, 0.32 %, and 1.6 m/s (0.65 m/s for $t > 40$ min) up to an altitude of 180 km.

(d) The upper boundary was slightly lowered by setting $M = 604$ (then, $D \sim 213$ km). The differences of n^α, T, and v_1^α up to an altitude of 140 km were less than 0.56 %, 4.6 %, and 3.4 m/s (0.001 %, 0.01 %, and 0.01 m/s for $t > 40$ min) in Case 1 and less than 0.01 %, 0.05 %, and 0.06 m/s in Case 2.

As seen above, rather large differences may occur in some cases especially at higher altitudes and during the first 40 min (i.e., while the waves in the profiles of the macroscopic quantities are running upward as seen in Figs. 3 and 9). However, those differences tend to decrease at lower altitudes. Besides, the column density of SO_2 obtained in the above tests does not differ from that shown in Fig. 13(a) by more than 0.08 %.

References

Andries, P., Aoki, K., Perthame, B., 2002. A consistent BGK-type model for gas mixtures. J. Stat. Phys. 106, 993–1018.

Aoki, K., Sone, Y., Yamada, T., 1990. Numerical analysis of gas flows condensing on its plane condensed phase on the basis of kinetic theory. Phys. Fluids A 2, 1867–1878.

Aoki, K., Takata, S., Kosuge, S., 1998. Vapor flows caused by evaporation and condensation on two parallel plane surfaces: Effect of the presence of a noncondensable gas. Phys. Fluids 10, 1519–1533.

Aoki, K., Takata, S., Taguchi, S., 2003. Vapor flows with evaporation and condensation in the continuum limit: Effect of a trace of noncondensable gas. Eur. J. Mech. B/Fluids 22, 51–71.

Austin, J. V., Goldstein, D. B., 2000. Rarefied gas model of Io's sublimation-driven atmosphere. Icarus 148, 370–383.

Ballester, G. E., Mcgrath, M. A., Strobel, D. F., Zhu, X., Feldman, P. D., Moos, H. W., 1994. Detection of the SO_2 atmosphere on Io with the Hubble Space Telescope. Icarus 111, 2–17.

Ballester, G. E., Moos, H. W., Feldman, P. D., Strobel, D. F., Summers, M. E., Bertaux, J.-L., Skinner, T. E., Festou, M. C., Lieske, J. H., 1987. Detection of neutral oxygen and sulfur emissions near Io using IUE. Astrophys. J. 319, L33–L38.

Bhatnagar, P. L., Gross, E. P., Krook, M., 1954. A model for collision processes in gases. I. Small amplitude processes in charged and neutral one-component systems. Phys. Rev. 94, 511–525.

Chu, C. K., 1965. Kinetic-theoretic description of the formation of a shock wave. Phys. Fluids 8, 12–22.

Clarke, J. T., Ajello, J., Luhmann, J., Schneider, N., Kanik, I., 1994. Hubble-Space-Telescope UV spectral observations of Io passing into eclipse. J. Geophys. Res. 99, 8387–8402.

de Pater, I., Roe, H., Graham, J. R., Strobel, D. F., 2002. Detection of the forbidden SO $a^1\Delta \to X^3\Sigma^-$ rovibronic transition on Io at 1.7 μm. Icarus 156, 296–301.

Douté, S., Schmitt, B., Lopes-Gautier, R., Carlson, R., Soderblom, L., Shirley, J., Galileo NIMS Team, 2001. Mapping SO_2 frost on Io by the modeling of NIMS hyperspectral images. Icarus 149, 107–132.

Fanale, F. P., Brown, R. H., Cruikshank, D. P., Clake, R. N., 1979. Significance of absorption features in Io's IR reflectance spectrum. Nature 280, 761–763.

Geissler, P., McEwen, A., Porco, C., Strobel, D., Saur, J., Ajello, J., West, R., 2004. Cassini observations of Io's visible aurorae. Icarus 172, 127–140.

Howell, R. R., Nash, D. B., Geballe, T. R., Cruikshank, D. P., 1989. High-resolution infrared spectroscopy of Io and possible surface materials. Icarus 78, 27–37.

Ingersoll, A. P., 1989. Io meteorology: How atmospheric-pressure is controlled locally by volcanos and surface frosts. Icarus 81, 298–313.

Ingersoll, A. P., Summers, M. E., Schlipf, S. G., 1985. Supersonic meteorology of Io: Sublimation-driven flow of SO_2. Icarus 64, 375–390.

Jessup, K. L., Spencer, J. R., Ballester, G. E., Howell, R. R., Roesler, F., Vigel, M., Yelle, R., 2004. The atmospheric signature of Io's Prometheus plume and anti-jovian hemisphere: Evidence for a sublimation atmosphere. Icarus 169, 197–215.

Kliore, A. J., Fjeldbo, G., Seidel, B. L., Sweetnam, D. N., Sesplaukis, T. T., Woiceshyn, P. M., Rasool, S. I., 1975. The atmosphere of Io from Pioneer 10 radio occultation measurements. Icarus 24, 407–410.

Lellouch, E., Belton, M., Depater, I., Gulkis, S., Encrenaz, T., 1990. Io's atmosphere from microwave detection of SO_2. Nature 346, 639–641.

Lellouch, E., Strobel, D. F., Belton, M. J. S., Summers, M. E., Paubert, G., Moreno, R., 1996. Detection of sulfer monoxide in Io's atmosphere. Astrophys. J. 459, L107–L110.

Moore, C. H., Goldstein, D. B., Varghese, P. L., Trafton, L. M., Stewart, B., 2009. 1-D DSMC simulation of Io's atmospheric collapse and reformation during and after eclipse. Icarus 201, 585–597.

Moreno, M. A., Schubert, G., Baumgardner, J., Kivelson, M. G., Paige, D. A., 1991. Io's volcanic and sublimation atmospheres. Icarus 93, 63–81.

Ohwada, T., Sone, Y., Aoki, K., 1989. Numerical analysis of the shear and thermal creep flows of a rarefied gas over a plane wall on the basis of the linearized Boltzmann equation for hard-sphere molecules. Phys. Fluids A 1, 1588–1599.

Pearl, J., Hanel, R., Kunde, V., Maguire, W., Fox, K., Gupta, S., Ponnamperuma, C., Raulin, F., 1979. Identification of gaseous SO_2 and new upper limits for other gases on Io. Nature 280, 755–758.

Retherford, K. D., Spencer, J. R., Stern, S. A., Saur, J., Strobel, D. F., Steffl, A. J., Gladstone, G. R., Weaver, H. A., Cheng, A. F., Parker, J. W., Slater, D. C., Versteeg, M. H., Davis, M. W., Bagenal, F., Throop, H. B., Lopes, R. M. C., Reuter, D. C., Lunsford, A., Conard, S. J., Young, L. A., Moore, J. M., 2007. Io's atmospheric response to eclipse: UV aurorae observations. Science 318, 237–240.

Smyth, W. H., Wong, M. C., 2004. Impact of electron chemistry on the structure and composition of Io's atmosphere. Icarus 171,

171–182.
Sone, Y., 2002. Kinetic Theory and Fluid Dynamics. Birkhäuser, Boston.
Sone, Y., 2007. Molecular Gas Dynamics: Theory, Techniques, and Applications. Birkhäuser, Boston.
Sone, Y., Onishi, Y., 1978. Kinetic theory of evaporation and condensation – Hydrodynamic equation and slip boundary condition –. J. Phys. Soc. Jpn. 44, 1981–1994.
Spencer, J. R., Jessup, K. L., McGrath, M. A., Ballester, G. E., Yelle, R., 2000. Discovery of gaseous S_2 in Io's Pele plume. Science 288, 1208–1210.
Spencer, J. R., Lellouch, E., Richter, M. J., Lopez-Valverde, M. A., Jessup, K. L., Greathouse, T. K., Flaud, J. M., 2005. Mid-infrared detection of large longitudinal asymmetries in Io's SO_2 atmosphere. Icarus 176, 283–304.
Strobel, D. F., Zhu, X., Summers, M. E., 1994. On the vertical thermal structure of Io's atmosphere. Icarus 111, 18–30.
Wagman, D. D., 1979. Sublimation pressure and enthalpy of SO_2. Chem. Thermodyn. Data Cent., Natl. Bur. of Stand., Washington, DC.
Walker, A. C., 2012. A comprehensive numerical model of Io's chemically-reacting sublimation-driven atmosphere and its interaction with the Jovian plasma torus. Ph.D. thesis, University of Texas at Austin.
Walker, A. C., Gratiy, S. L., Goldstein, D. B., Moore, C. H., Varghese, P. L., Trafton, L. M., Levin, D. A., Stewart, B., 2010. A comprehensive numerical simulation of Io's sublimation-driven atmosphere. Icarus 207, 409–432.
Walker, A. C., Moore, C. H., Goldstein, D. B., Varghese, P. L., Trafton, L. M., 2012. A parametric study of Io's thermophysical surface properties and subsequent numerical atmospheric simulations based on the best fit parameters. Icarus, submitted for publication.
Welander, P., 1954. On the temperature jump in a rarefied gas. Ark. Fys. 7, 507–553.
Wong, M. C., Johnson, R. E., 1995. The effect of plasma-heating on sublimation-driven flow in Io's atmosphere. Icarus 115, 109–118.
Wong, M. C., Johnson, R. E., 1996. A three-dimensional azimuthally symmetric model atmosphere for Io. 1. Photochemistry and the accumulation of a nightside atmosphere. J. Geophys. Res. 101, 23243–23254.
Wong, M. C., Smyth, W. H., 2000. Model calculations for Io's atmosphere at eastern and western elongations. Icarus 146, 60–74.
Zhang, J., Goldstein, D. B., Varghese, P. L., Gimelshein, N. E., Gimelshein, S. F., Levin, D. A., 2003. Simulation of gas dynamics and radiation in volcanic plumes on Io. Icarus 163, 182–197.